COBEM 2021 26th International Congress of Mechanical Engineering
ABCM Associação Brasileira de Engenharia e Ciências Mecânicas
November 22-26, 2021, Virtual Congress, Brazil

COB-2021-0061
SOOT PRECURSORS ANALYSYS USING DETAILED CHEMICAL KINETIC MECHANISMS IN AN ETHYLENE/AIR LAMINAR DIFFUSION FLAME

Sebastián Ruiz, Cesar Celis
Mechanical Engineering Section, Pontificia Universidad Católica del Perú
Av. Universitaria 1801, San Miguel, Lima 32, Lima, Peru
sebastian.ruiz@pucp.edu.pe, ccelis@pucp.edu.pe

Luís Fernando Figueira da Silva
Deparment of Mechanical Engineering, Pontifícia Universidade Católica do Rio de Janeiro
Rua Marquês de São Vicente 225, Rio de Janeiro, RJ 22451-900, Brazil
luisfer@puc-rio.br

Abstract. *Tens or even hundreds of chemical species are produced in the nascent stages of hydrocarbon-based fuels combustion that eventually lead to the formation of soot particles and aggregates. In such context, the study of soot-related chemical species formation and its associated physical-chemical phenomena are of great importance to delve into how in combustion processes the formation of this critical pollutant is carried out. In this work thus, accounting for an ethylene/air laminar diffusion flame previously experimentally characterized employing a Gülder burner configuration, both soot precursors and soot formation are analyzed. Computational mesh independence is addressed here by refining grid elements in such a way that element sizes in the reaction zone are of about 30μm, thus capturing species and temperature gradients in such regions. The NBP (Narayanaswamy, Blanquart and Pitsch Stanford University mech) chemical kinetic mechanism featuring 149 chemical species and 1651 reactions is used for describing gas phase chemistry. Radiation effects are addressed using the discrete ordinates method (DOM) and computing the associated absorption coefficient from a WSGG model. Two soot formation models, an acetylene-based semiempirical and a statistical PAH-based method of moments (MOM), are employed in the soot-related numerical simulations carried out. Temperature profiles predicted using the MOM soot formation model are in fair agreement with the experimental results (peak temperature discrepancies of about 3%). Along the flame centerline and near the burner surface, predicted soot volume fractions match as well the corresponding experimental trends. In the radial direction however, both models lack of precision for describing the soot peak values and their physical location. From the species molar fractions results discussed here, it is observed that one and two aromatic ring groups are the most abundant PAH, so these PAH might be sufficient for soot nucleation purposes. The numerical models and methodologies developed in this work will be used in future for predicting soot formation in turbulent diffusion flames.*

Keywords*: Soot precursors, Detailed kinetic mechanisms, PAH, Soot modeling, Laminar diffusion flames*

1. INTRODUCTION

Soot is generated by the condensation of a wide variety of gaseous chemical species, which in turn are formed by the pyrolysis and incomplete combustion of hydrocarbon fuels. More specifically, soot consists of particles and fractal structured aggregates, ranging in size from nanometer to micrometer scales (Rigopoulos, 2019). Emissions of particulate matter and other pollutants are of great concern to mankind because of their known detrimental effects on both health and environment. Among the undesired combustion products, polycyclic aromatic hydrocarbons (PAH), molecules playing a key role in soot formation processes, have been reported to interact with DNA and being carcinogenic (Baird et al., 2005). It is also worth noticing that research in soot formation processes is driven by not only the endeavor of reducing people's carbon footprint, but also the need to both improve efficiency of practical combustion devices and fill the knowledge gaps about PAH evolution and soot formation.

Computational fluid dynamics (CFD) based modeling of soot formation in laminar diffusion flames generally involves the use of a chemical kinetic mechanism, as well as soot formation and radiation models. Firstly, chemical kinetic mechanisms include in particular the description of the thermochemical and transport phenomena characterizing the flames. They are frequently developed and validated for a specific fuel or fuels with a range of molecular mass, so a differentiation for the particular application is initially required. A review of chemical kinetic mechanisms for different fuel applications is provided by Konnov et al. (2018). Detailed kinetic mechanisms describing the combustion of C1-C4 fuels include for instance, ABF (Appel et al., 2000), NBP (Narayanaswamy et al., 2010), DLR (Slavinskaya et al., 2019), USCII (Wang et al., 2007) and KM2 (Wang et al., 2013). These mechanisms include at least the formation of aromatics

with one to two rings. Secondly, over the years soot numerical description has evolved from the early empirical and semi-empirical models to the more advanced statistical ones. The first successful semi-empirical models attempt to capture soot volume fraction within the same order of magnitude as the associated experimental data by considering acetylene as its main precursor. Statistical models in turn include a more detailed description of the soot formation mechanisms and are capable of describing in a limited sense parameters related to soot particles morphology, such as the primary particle diameter and the particle size distribution. Latter models include those based on the method of moments (Frenklach, 2002), the sectional method (Netzell et al., 2007), and the Monte Carlo stochastic one (Balthasar and Kraft, 2003). As highlighted by the multi-moment sectional method (Yang and Mueller, 2019), in which statistical moments are computed for each domain section, hybridization of the referred soot modeling approaches is possible as well. Since the utilization of less general semi-empirical models involves a relatively low computational cost, its use in recent years has been mainly limited to complex applications, including turbulent flows (Reddy et al., 2016; Snegirev et al., 2018), practical compression ignition engines (Martos et al., 2018), and laminar flows including detailed chemistry (Johnson et al., 2020). Detailed soot formation models can be also used in similar applications but the computational cost is comparatively higher. Detailed soot models related works therefore focus on more comprehensive analyses of soot evolution mechanisms and morphology in simpler flame configurations (Zhang et al., 2019; Gleason et al., 2021). Finally, regarding the use of radiation models, simplified models such as P1 or more expensive ones such as those based on the discrete ordinate method (DOM) are commonly used to solve the radiative transfer equation (RTE). The former is a rather crude model, but it has limitations when capturing radiation directional variations, which may be present in optically thin mediums (Modest and Haworth, 2016). As for the radiative properties, the absorption coefficient is frequently computed through the weighted sum of grey gases (WSGG) model, which is a global model representing radiative effects through fictitious gases. The main disadvantage of this model is its dependence on the emissivity coefficient, which could lead to inaccurate results in close proximity to combustion systems walls (Yadav et al., 2013)

Accordingly, this work aims to study the formation of soot in laminar diffusion flames and the major chemical species and PAH formed during the associated combustion process. As carried out in recent studies (Jerez et al., 2019; Gleason et al., 2021), this is performed by analyzing the reaction rates and computed mass fractions. What differentiates this work from previous ones is the type of two-dimensional configuration-based analyses carried out here and the use of different soot formation models. Furthermore, it is of particular interest to the authors the development of a suitable approach for carrying out in future sooting flames related research. Challenges faced during the modeling of the laminar diffusion flames studied here include (i) the fine mesh required to capture the relatively fast chemical species mass fractions, (ii) the implementation of the previously mentioned soot detailed models, and (iii) the high computational cost representing the solution of the stiff detailed chemistry, involving the computing of hundreds of chemical species and hundreds/thousands of chemical reactions. Following this brief introduction, the mathematical models utilized here are described in Section 2. In Section 3, the geometric configuration, the computational mesh and the numerical methods accounted for are highlighted. Next in Section 4 results and discussions are presented. Finally, some conclusions are provided in Section 5.

2. MATHEMATICAL MODELING

In this section the main mathematical models accounted for in this work are briefly described. Governing equations are firstly discussed, followed by the soot formation models and the radiation ones employed here.

2.1. Governing equations

Laminar flows with variable density are accounted for in this work. Accordingly, transport equations for mass, momentum, energy and chemical species in an axisymmetric reference frame are solved. For the sake of brevity however these equations are not explicitly depicted here, their derivation is available in (Law, 2006; Poinsot and Veynante, 2012). For the computation of the species equation chemical reaction term, species source and sink are determined by using the NBP chemical kinetic mechanism (Blanquart et al., 2009; Narayanaswamy et al., 2010). This mechanism includes 153 chemical species and 1350 chemical reactions, as well as the main reaction paths for small aliphatic species, benzene and PAH growth up to four ringed compounds.

2.2. Soot models

Two soot formation models, the semi-empirical Brookes and Moss model (1999) and the method of moments with interpolative closure (MOMIC) one (Frenklach, 2002) are assessed here. The semi-empirical model involves the solution of two transport equations for soot mass fraction and nuclei concentration,

$$\frac{\partial \rho b_{nuc}}{\partial t} + \nabla \cdot (\rho \bar{v})\, b_{nuc} = \nabla \cdot \left(\frac{\mu_{eff}}{\sigma_{nuc}} \nabla b_{nuc} \right) + \frac{1}{N_{norm}} \frac{dN}{dt}, \tag{1}$$

$$\frac{\partial \rho Y_{soot}}{\partial t} + \nabla \cdot (\rho \vec{v}) Y_{soot} = \nabla \cdot \left(\frac{\mu_{eff}}{\sigma_{soot}} \nabla Y_{soot} \right) + \frac{dM}{dt}, \tag{2}$$

where b_{nuc} is the normalized soot radical nuclei concentration, Y_{soot} the soot mass fraction, N the soot particle number density and M represents the soot mass concentration. Also ρ, $\bar{v}$ μ_{eff}, σ_{soot}, σ_{nuc} stand for, respectively, density, velocity, effective viscosity and Prandtl number for soot transport and nuclei transport.

In the Brookes and Moss model, specifically, soot number density and soot mass concentration source terms are proportional to the acetylene mass fraction. Moreover, soot number density is defined by means of nucleation and coagulation, whereas the soot mass fraction source term includes nucleation, surface growth and oxidation. In this work soot oxidation is computed using the Lee oxidation model (Lee et al., 1962), as it accounts for oxidation due to both OH and O_2. Notice that in the referred equations empirical scaling factors and other model parameters are used to give a better data fit. These parameters were originally determined by Brookes and Moss (1999) accounting for a methane-air diffusion flame.

The method of moments utilized here uses a Lagrange interpolation for the closure of the moments-related source terms. When using this model, the steps in soot evolution are modeled as follows. Soot nucleation involves the coalescence of PAH, coagulation features the collision and union of two particles, and surface growth and oxidation include in turn surface reactions of soot with acetylene, hydroxyl radical and molecular oxygen. In particular, for each moment, a transport equation of the form,

$$\frac{\partial \rho (M_r)}{\partial t} + \nabla \cdot (\rho \vec{v}) M_r = \nabla \cdot \left(\frac{\mu_{eff}}{\sigma_{MOM}} \nabla M_r \right) + \frac{dM_r}{dt}, \tag{3}$$

is solved, in which the different referred soot evolution mechanisms are accounted for. In Eq. (3) M_r stands for the r-th moment of the soot size distribution, μ_{eff} is the effective diffusion coefficient, σ_{MOM} is the Prandtl number for the moment transport equation, and dM_r/dt is the r-th moment source term. This last term is in turn computed as,

$$\frac{\mathrm{d}M_r}{dt} = R_r + G_r + W_r. \tag{4}$$

where R_r, G_r, W_r are the inception, coagulation and surface growth and oxidation source terms, respectively. Notice that the zeroth moment M_0 accounts for nucleation and coagulation source terms only. Higher order moments provide a more accurate description of the particle size distribution, and thus takes into account all three R, G and W source terms. For full description of each of these source terms the interested reader may refer to (Frenklach 2002; Rigopoulos, 2019).

2.3. Radiation models

The radiation model used here to solve the RTE is the discrete ordinates method (DOM) one. It involves the solution of a transport equation for each direction vector, which is a quantity proportional to the solid angles considered for the spatial discretization. The medium is treated as optical thin and the effects of scattering phenomena are neglected. Under these assumptions, the total gas emissivity and absorption coefficients are calculated with the weighted sum of grey gases (WSGG) model (Yadav et al., 2013). Accordingly, the gas emissivity coefficient is computed as,

$$\varepsilon_g = \sum_{i=0}^{N_g} a_{\varepsilon,i}(T)[1 - e^{-k_i ps}] \tag{5}$$

and the gas absorption coefficient from,

$$a_g = -\frac{\ln(1 - \varepsilon_g)}{s} \tag{6}$$

where N_g iz the number of fictitious gray gases, $a_{\varepsilon,i}(T)$ and k_i are, respectively, the emissivity weighting factor and the absorption coefficient for the ith gray gas. In addition, p is the sum of the gray gases partial pressures and s the mean beam length. Notice that the a_i values are calculated as a polynomial function of temperature, whereas each polynomial coefficient and k_i are determined by fitting them to a library of total emissivities (Smith et al., 1982).

3. NUMERICAL APPROACH

In this section the mean features of the numerical approach employed here are briefly described.

3.1 Numerical methods

In this work ANSYS Fluent (ANSYS, 2021a) was used to solve the set of governing equations utilized. The PISO algorithm was used for the velocity-pressure coupling. Additionally, a second order upwind scheme was used for the

mass, momentum and species equations spatial discretization. The least squares cell-based method was used in turn for the evaluation of gradients and derivatives, and a PRESTO! (Pressure staggering option) scheme was employed for the pressure interpolation. Moreover, a direct use of finite-rate chemical kinetics was considered for obtaining the source term of the species transport equation, neglecting the effects of turbulence on the reaction rates. The pseudo-transient under-relaxation method together with the ISAT tool (Pope, 1997) was used to accelerate the transition from flame initialization to a condition close to the final stable flame. ISAT tolerance errors were progressively reduced, starting with 10^{-3} and 10^{-4}, seeking for stabilization of maximum temperatures and residuals. As this was not achieved for smaller tolerance error values, direct integration was used for reaching the final result.

3.2 Computational domain and boundary conditions

The flame studied here corresponds to a laminar ethylene/air diffusion flame stabilized in a coflow configuration (Figure 1a). The particular burner associated with this flame is the canonical Gülder one (Snelling et al., 1999), in which a sooty flame is stabilized. The fuel duct has a diameter of 10.65mm, whereas the outer air duct has a diameter of 99.90mm. Additionally, the inner duct wall has a width of 1mm. The fuel flow rate corresponds to 0.1 slpm, whereas the air flow rate value is 60 slpm.

The experimental data used here for comparison and validation purposes was obtained by Jerez et al. (2019), where soot volume fraction and other soot related parameters were measured. In particular, measurements were carried out by simultaneous laser induced incandescence (LII) and planar laser induced fluorescence (PLIF) techniques for four different wavelengths 340, 400, 450 and 550nm. Each wavelength was associated to a particular PAH group, based on the hypothesis that species with similar molecular mass fluoresce in the same spectral band. Additionally, measurements of temperature fields were performed by means of a two color pyrometry technique.

3.3 Mesh adaptions

In order to obtain in the flame reactive zone a sufficiently refined mesh not affecting the computed flow properties, several mesh refinements progressively featuring finer meshes were performed. The initial mesh featured about 20,000 elements, whereas the final one did so almost 90,000 elements. The referred refinements involved mesh adaptions based on global scaled gradients of selected chemical species such as C_2H_6, C_3H_3 and OH. The corresponding normalized threshold values employed in such mesh refinement processes ranged from 0.1 to 0.01, which were chosen by considering the quality of the progressively obtained results (da Costa Ramos et al., 2020). Final stages of the mesh adaptions processes carried out are shown in Figure 1b, where the smallest mesh element features a size of roughly 30µm.

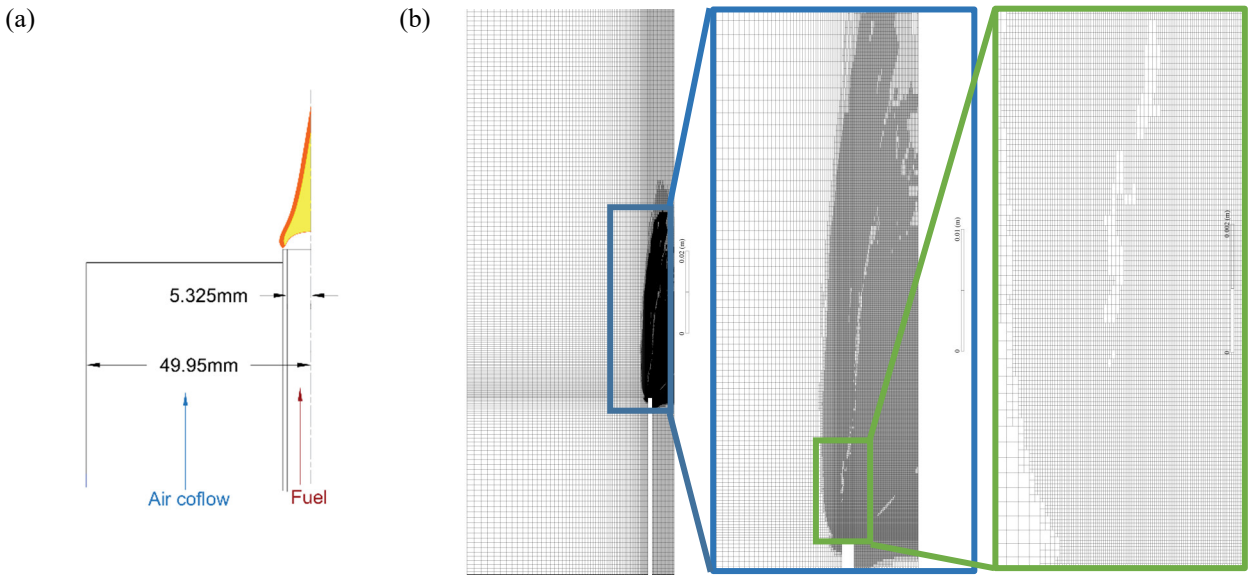

Figure 1. (a) Scheme of Gülder burner. (b) Computational mesh generated in ANSYS Meshing (ANSYS, 2021b) and adapted in ANSYS Fluent (ANSYS, 2021a).

4. RESULTS AND DISCUSSION

In this section two sets of results are presented and discussed. In both set of results the same mathematical models and numerical methods were used, excepting the soot model. The first and second sets of results were obtained using the Moss and Brookes semi-empirical model and the MOMIC one, respectively. Firstly, numerical results are compared with

experimental data of Jerez et al. (2019), accounting for temperature and soot volume fractions contours and profiles. Then, based on their computed mole fractions and reaction rates, gas phase aliphatic precursors and PAH gathered by their number of rings are analyzed.

4.1 Results validation

Figure 2 qualitatively compares the computed temperature and soot volume fraction with the corresponding experimental data. Figure 2a and c correspond to the semi-empirical Brookes and Moss model, and Figure 2b and d do so to the MOMIC one. From this figure it can be firstly seen that the computed temperature distributions (Figure 2a and b), are qualitatively similar to the one characterizing the experimental flame, being the region of maximum temperatures located in the flame wings. In the experimental case however, this maximum temperature region is found at a higher position above the burner. In addition, when using the semi-empirical and MOMIC models here, temperature maximum values are underestimated by 4.5% and 3%, respectively. Figure 2b and d show in turn that the experimental soot volume fraction field has not been well reproduced with the soot formation models employed here. Qualitatively, soot distributions are far from having a similar trend to what is experimentally observed. It is noticed that for both the semi-empirical and the method of moments, soot volume fraction peaks in the central region of the flame, whereas in the experimental case, this occurs in the flame wings. Moreover, peak soot volume fractions values are underestimated by about 34% and 67% (Figure 2c and d).

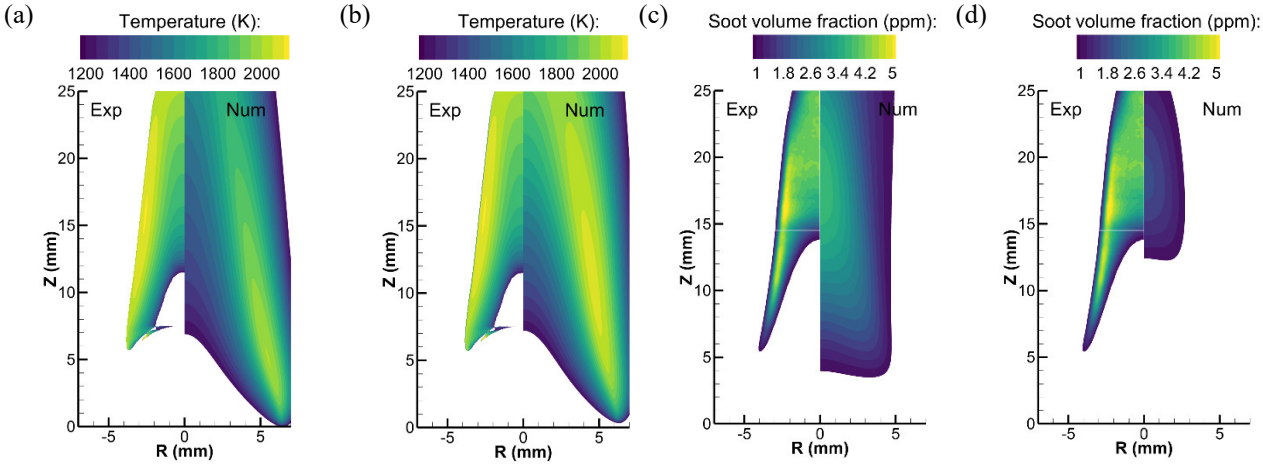

Figure 2. Temperature (left plots) and soot volumetric fraction (right plots) contours for the semi-empirical model [(a) and (c)], and the MOMIC one [(b) and (d)]. Experimental data (Jerez et al., 2019) shown on the left side of each plot.

Temperature and soot volume fraction axial and radial profiles along the burner centerline and at a normalized flame height of Z/H=0.6 are shown in Figure 3. Notice that following Jerez et al. (2019), the experimental flame height (H) is defined here as the Z coordinate where the CH* self-emitted chemiluminescence is observed. In Figure 3, square symbols, dashed and dash-dot-dotted lines represent, respectively, experimental data, semi-empirical and MOMIC models results, both including radiation. Additionally, the solid line in Figure 3a corresponds to the "initial" simulation without soot and radiation models. From Figure 3a and b it is observed that, in terms of temperature, the computed results including both soot and radiation models match the corresponding experimental curve slope along the flame centerline and radial direction. The computed temperature values are however lower than the measurements, whose uncertainty is 16% (290K) (Jerez et al., 2019). Moreover, along the centerline, the semi-empirical and MOMIC models underestimate temperature peak values in 16% and 4%, respectively. Whereas, in the radial direction, peak temperature values are underestimated by about 12% and 3%.

In terms of soot volume fraction, Figure 3c and d show discrepancies similar to what was previously observed in qualitative terms (Figure 2). Indeed, it is noticed from Figure 3d that when using the semi-empirical and MOMIC models the peak value of the experimental soot volume fraction, which uncertainty is about 30%, is underestimated by 22% and 65%, respectively. Soot volume fraction trends are not well reproduced either. In fact, from the radial profiles (Figure 3d), it is noticed that the position of the soot peak values in the experimental data is found farther away from the center, which does not occur in the case of the numerical soot predictions carried out. It is also worth emphasizing that, by changing the surface growth source term in the semi-empirical model, it was possible to obtain along the centerline a soot volume fraction peak value similar to the experimental one. This change also affected however the calculated soot mass fraction, which in turn is used to compute the soot absorption coefficient. So major differences found in the temperature fields for this case could be originated by this fact. In addition, in order to assess model formulations and their influence on soot predictions when using semi-empirical soot models, the laminar flame studied by Zimmer and Pereira (2020) was

also evaluated using the models used in the present work. The results not included here for the sake of brevity indicated that the soot volume fraction fields are completely different to the ones discussed in the original work (Zimmer and Pereira, 2020). This happened even though the soot source terms regarding nucleation, surface growth and oxidation showed similar trends. Therefore, from the comparison of the models used in both works, it can be inferred that possible sources of errors when computing soot volume fractions may come from both not considering thermophoresis effects in the soot transport equations, and not correctly coupling precursors mass fractions to soot formation. Thermophoresis is a diffusion phenomenon transporting soot particles to flame regions of high temperature gradients. Not accounting for soot precursors mass fraction reduction due to soot formation may also influence soot volume faction predicted profiles.

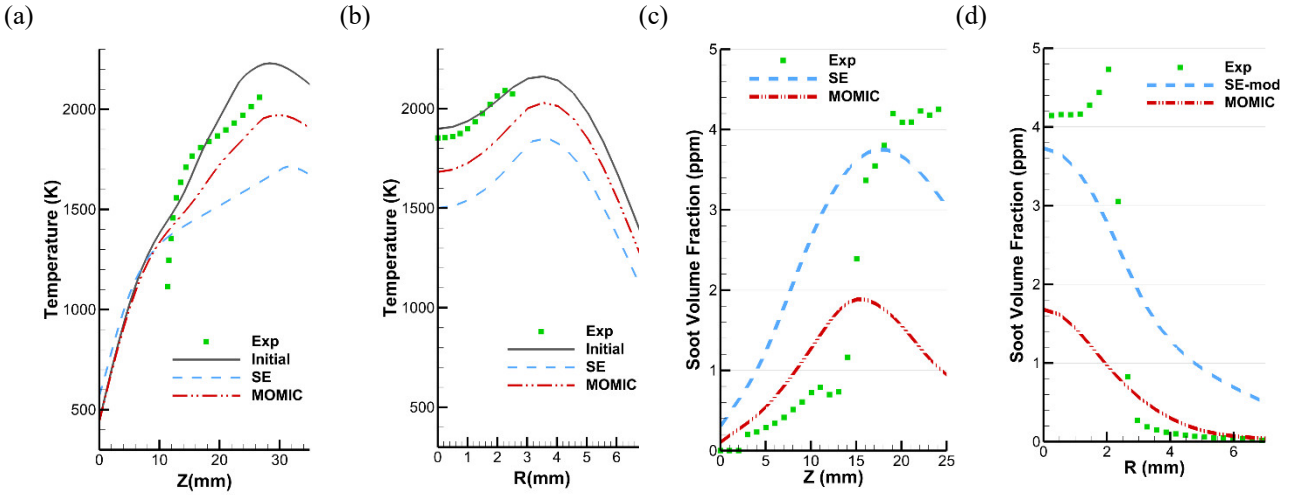

Figure 3. Temperature (left) and soot volumetric fraction (right) profiles along the centerline (a) and (c) and the radial direction (b) and (d). In this figure, Exp, SE and MOMIC correspond to, respectively, experimental data, semi-empirical with radiation, MOMIC with radiation.

4.2 Soot precursors analysis

The case used for this analysis is the one associated with the use of MOMIC and DO radiation models. Due to soot fields were not well reproduced with the soot models employed here, only the experimental soot volume fraction is accounted for in this section. Accordingly, in Figure 4a and c, aliphatic soot precursors and PAH mole fractions along the flame normalized height (Z/H) are shown. For a better visualization of the different orders of magnitude characterizing each chemical species, the vertical coordinates use logarithm scales. In particular, Figure 4a shows the major gas phase species that participate in the formation of the first ring included in the kinetic mechanism used in this work. Whereas Figure 4b shows the kinetic rate of the main chemical reactions leading to the formation of benzene.

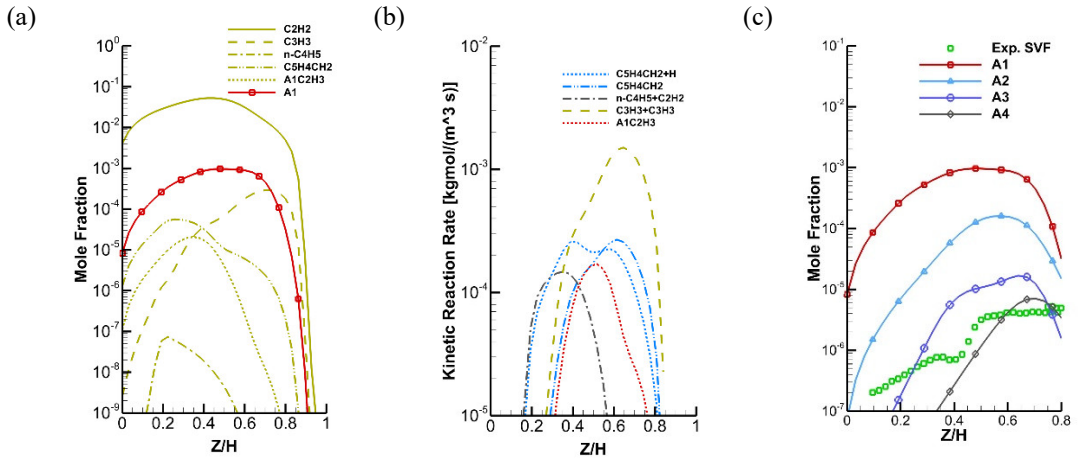

Figure 4. Species mole fractions results along the flame normalized height. (a) Aliphatic soot precursors and (b) PAH. Experimental soot volume fractions (green symbols) are included in the right plot as well.

According to Figure 4a, for the particular flame studied here, acetylene maintains high concentration values along the flame development, fulvene ($C_5H_4CH_2$) concentration peaks at Z/H=0.32 and propargyl (C_3H_3) is found to peak at Z/H=0.71. These results, along with those ones seen in Figure 4b, seem to suggest that fulvene related reaction paths may be favored over early stages of the flame, whereas as the flame approaches to the oxidation zone, benzene formation may come from the recombination of propargyl. From Figure 4b it can also be seen that the acetylene reaction with the C_4H_5 radical may play an important role in the early stages of the flame. Although the concentration of n-C4H5 is not significant indeed (below 10^{-6}), it can be related to its high consumption. Acetylene reactions with other radicals to form benzene or directly phenyl may not be favored at the centerline of flame, as their reaction rates are not found to be significant. Nevertheless, it is likely that these reactions take place in other regions of the flame, such the flame wings, which are not seen here. Figure 4c shows in turn the main PAH (C_6H_6, $C_{10}H_8$, $C_{14}H_{10}$ and $C_{16}H_{10}$) included in the chemical kinetic mechanism utilized here. Notice that in this work A1, A2, A3 and A4, stand for, respectively, benzene, naphthalene, phenanthrene and pyrene. From Figure 4b and c can be observed then, to form benzene (A1) in the flame later stages, the dominant reaction paths may be related to the recombination of propargyl. Observing Figure 4c indeed, from A1 to A4, each PAH peaks at Z/H equal to 0.5, 0.58, 0.65 and 0.7, respectively. In a similar fashion, the experimental measured soot volume fractions peak in the Z/H range between 0.58 and 0.8, which agrees with the range of Z/H values where the PAH peak values are found (Figure 4c). This outcome seems to suggest that the discrepancies between the experimental and computed soot volume fractions highlighted before may not come from the description of the chemical species involved, but from the soot formation models accounted for. Notice as well that, as expected, PAH peak concentration values progressively decrease with each aromatic ring addition (Li et al., 2021).

Finally, following Jerez et al. (2019), Figure 5 shows mole fractions along the flame normalized height (Z/H) of PAH grouped by their number of aromatic rings. According to this figure, the PAH most abundant species for each aromatic group are benzene, naphthalene, acenaphthylene (A2R5), phenanthrene and pyrene. It is also worth noticing that the most abundant PAH peak at the Z/H range between 0.6 and 0.8, which is again consistent with the experimental soot concentration peak locations seen in Figure 4c. Peak mole concentrations for the referred PAH are indeed 945, 260, 18.9 and 7 ppm, respectively. These results are also in good agreement to what was observed in the work by Gleason et al. (2021), where it was concluded that the most significant aromatics that should be taken into account for soot nucleation are the one and two ringed aromatic compounds. It is also worth emphasizing that aromatic compounds with five-membered ring insertions (A2R5, A3R5 and A4R5) feature concentrations comparable to six-membered ring structure PAH (A2, A3 and A4). This last result highlights the importance (at least for flames as the one accounted for here) of five-membered ring PAH, and their relevance for both PAH growth (Schulz et al., 2019) and curvature (Wang and Chung, 2019).

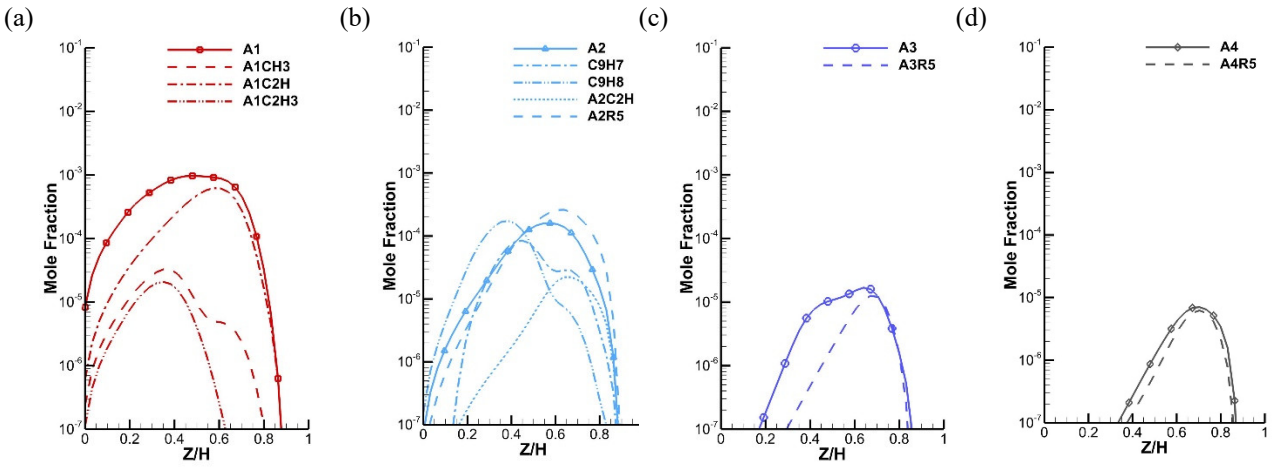

Figure 5. Mole fractions of PAH grouped by (a) one, (b) two, (c) three and (d) four aromatics rings.

5. CONCLUSIONS

In this work two soot formation models were assessed and their associated results were compared to measurements available in literature. It was found that the temperature profiles predicted using the detailed soot model is in fair agreement with the experimental results, within their experimental uncertainty (16%, 290K). When using the MOMIC model with radiation, temperature peak values were underestimated indeed by about 3% only. This highlights the capabilities of both the NBP gas-phase chemical kinetic mechanism and the DOM radiation model employed here for numerical modeling this fuel type and the flame conditions studied here. In addition, along the flame centerline, soot volume fractions predicted using the semi-empirical soot formation model matched the experimental peak value. For the radial profiles however, both semi-empirical and MOMIC models lacked of precision for describing the soot peak values and their physical location. Contrarily to what is observed in the numerical results indeed, measurements indicate that

this location is found over the flame wings. Following the radial direction indeed, when using the simplified and detailed soot models, soot volume fraction predictions were underestimated by 22% and 65%, respectively. In accordance with previous works, for this particular ethylene air-diffusion flame, it was found that relevant soot precursors are those chemical species related to acetylene, as well as to radicals such as propargyl. Fulvene and propargyl reactions were found to dominate indeed benzene formation over the first stages of the flame. From the species molar concentration results discussed here, it is possible to conclude that one and two aromatic ring groups are the most abundant PAH, so these PAH might be sufficient for soot nucleation purposes.

6. ACKNOWLEDGEMENTS

This work has been supported by CONCYTEC-FONDECYT (Peru), Contract No. 415-2019-2019-FONDECYT, "Identification of soot precursors in turbulent combustion processes through numerical modeling to reduce the impact of soot on both health and environment". During this work Luís Fernando Figueira da Silva was on leave from the Institut Pprime (CNRS - Centre National de la Recherche Scientifique, France). The authors also gratefully acknowledge the support provided by Brazil's Conselho Nacional de Desenvolvimento Cientifico e Tecnologico, CNPq, under the Research Grants No. 304444/2018-9 and 403904/2016-1.

7. REFERENCES

ANSYS Fluent, 2021a. ANSYS Inc., https://www.ansys.com/products/fluids/ansys-fluent. Accessed 21 June 2021.

ANSYS Mesh, 2021b. ANSYS Inc. https://www.ansys.com/products/meshing. Accessed 21 June 2021

Appel, J., Bockhorn H., and Frenklach M., 2000. "Kinetic Modeling of Soot Formation with Detailed Chemistry and Physics: Laminar Premixed Flames of C2 Hydrocarbons." *Combustion and Flame* 121(1–2):122–36.

Baird, W. M., Hooven L.A., and Mahadevan B., 2005. "Carcinogenic Polycyclic Aromatic Hydrocarbon-DNA Adducts and Mechanism of Action." *Environmental and Molecular Mutagenesis* 45(2–3):106–14.

Balthasar, M. and Kraft, M., 2003. "A Stochastic Approach to Calculate the Particle Size Distribution Function of Soot Particles in Laminar Premixed Flames." *Combustion and Flame* 133(3):289–98.

Blanquart, G., Pepiot-Desjardins, P., and Pitsch, H. (2009). "Chemical mechanism for high temperature combustion of engine relevant fuels with emphasis on soot precursors." *Combustion and Flame*, *156*(3):588–607.

Brookes, S. J. and Moss J.B., 1999. "Measurements of Soot Production and Thermal Radiation from Confined Turbulent Jet Diffusion Flames of Methane." *Combustion and Flame* 116(1–2):49–61.

Da Costa, L., R., Di Meglio, F., Figueira da Silva, L., F., and Morgenthaler, V. (2020). "Reduced Order Model of Laminar Premixed Inverted Conical Flames." *AIAA Scitech 2020 Forum* 2020-0416

Frenklach, M., 2002. "Method of Moments with Interpolative Closure." *Chemical Engineering Science* 57(12):2229–39.

Frenklach, M., Singh R., and Mebel, A.M., 2019. "On the Low-Temperature Limit of HACA." *Proceedings of the Combustion Institute* 37(1):969–76.

Gleason, K., Carbone, F., Sumner, A.J., Drollette, B.D., Plata, D.L. and Gomez, A., 2021. "Small Aromatic Hydrocarbons Control the Onset of Soot Nucleation." *Combustion and Flame* 223:398–406.

Jerez, A., Cruz, J.J., Figueira da Silva L.F., Demarco, R., and Fuentes, A., 2019. "Measurements and Modeling of PAH Soot Precursors in Coflow Ethylene/Air Laminar Diffusion Flames." *Fuel* 236:452–60.

Johnson, P.R., Chakrabarty, R.K., and Kumfer, B.M., 2020. "Evaluation of Semi-Empirical Soot Models for Nonpremixed Flames with Increased Stoichiometric Mixture Fraction and Strain: Evaluation of Semi-Empirical Soot Models." *Combustion and Flame* 219:70–85.

Konnov, A. A., Mohammad, A., Kishore, V. R., Kim, N. Il, Prathap, C., and Kumar, S., 2018. "A Comprehensive Review of Measurements and Data Analysis of Laminar Burning Velocities for Various Fuel+air Mixtures." *Progress in Energy and Combustion Science* 68:197–267.

Law, C.K., 2006. *Combustion Physics*. Cambridge University Press, New York.

Lee, K. B., Thring, M. W., and Beér, J. M.1962. "On the Rate of Combustion of Soot in a Laminar Soot Flame." *Combustion and Flame* 6:137–145.

Liu, A. and Rigopoulos, S., 2019. "A Conservative Method for Numerical Solution of the Population Balance Equation, and Application to Soot Formation." *Combustion and Flame* 205:506–21.

Martos, F. J., González, G.M., and Herreros J.M., 2018. "Semi-Empirical Model for Indirect Measurement of Soot Size Distributions in Compression Ignition Engines." *Measurement: Journal of the International Measurement Confederation* 124:32–39.

Modest, M.F. and Haworth D.C., 2016. *Radiative Heat Transfer in Turbulent Combustion Systems: Theory and Applications*.Springer, New York.

Narayanaswamy, K., Blanquart, G., and Pitsch, H., 2010. "A Consistent Chemical Mechanism for Oxidation of Substituted Aromatic Species." *Combustion and Flame* 157(10):1879–98.

Netzell, K., Lehtiniemi, H., and Mauss, F., 2007. "Calculating the Soot Particle Size Distribution Function in Turbulent Diffusion Flames Using a Sectional Method." *Proceedings of the Combustion Institute* 31(1):667–74.

Poinsot, T., and Veynante, D., 2012. *Theoretical and Numerical Combustion.* R.T.Edwards Inc., Philadelphia.

Pope, S. B. 1997. "Computationally Efficient Implementation of Combustion Chemistry Using in Situ Adaptive Tabulation." *Combustion Theory and Modelling* 1(1):41–63.

Reddy, B. M., De, A., and Yadav, R., 2016. "Numerical Investigation of Soot Formation in Turbulent Diffusion Flame with Strong Turbulence-Chemistry Interaction." *Journal of Thermal Science and Engineering Applications* 8(1):1–11.

Rigopoulos, S., 2019. "Modelling of Soot Aerosol Dynamics in Turbulent Flow." *Flow, Turbulence and Combustion* 103(3): 565–604.

Schulz, C., Kock, B. F., Hofmann, M., Michelsen, H., Will, S., Bougie, B., Suntz, R., and Smallwood, G., 2006. "Laser-Induced Incandescence: Recent Trends and Current Questions." *Applied Physics B: Lasers and Optics* 83(3):333–54.

Slavinskaya, N. A., and Frank, P., 2009. "A Modelling Study of Aromatic Soot Precursors Formation in Laminar Methane and Ethene Flames." *Combustion and Flame* 156(9):1705–22.

Slavinskaya, N., Mirzayeva, A., Whitside, Starke, R,H., Abbasi M., Auyelkhankyzy M.., and Chernov, V., 2019. "A Modelling Study of Acetylene Oxidation and Pyrolysis." *Combustion and Flame* 210:25–42.

Smith, T. F., Shen, Z. F., and Friedman, J. N., 1982. "Evaluation of Coefficients for the Weighted Sum of Gray Gases Model." *Journal of Heat Transfer* 104(4):602–8.

Snegirev, A., Markus, E., Kuznetsov, E., Harris, J., and Wu, T., 2018. "On Soot and Radiation Modeling in Buoyant Turbulent Diffusion Flames." *Heat and Mass Transfer/Waerme- Und Stoffuebertragung* 54(8):2275–93.

Snelling, D. R., Thomson, K. A., Smallwood, G. J., and Gülder, Ö. L., 1999. "Two-Dimensional Imaging of Soot Volume Fraction in Laminar Diffusion Flames." *Applied Optics* 38(12):2478.

Wang H., You, X., Joshi, A.V., Davis, S.G., Laskin, A., Egolfopoulos, F., and Law, C.K., 2007. "USC Mech Version II. High-Temperature Combustion Reaction Model of H2/CO/C1-C4 Compounds."

Wang, Y., Raj, A., and Chung, S. H., 2013. "A PAH Growth Mechanism and Synergistic Effect on PAH Formation in Counterflow Diffusion Flames." *Combustion and Flame* 160(9):1667–76.Yadav, R., Kushari, A., Verma, A. K., & Eswaran, V., 2013. "Weighted Sum of Gray Gas Modeling for Nongray Radiation in Combusting Environment Using the Hybrid Solution Methodology." *Numerical Heat Transfer, Part B: Fundamentals* 64(2):174–97.

Yang, S., and Mueller, M. E., 2019. "A Multi-Moment Sectional Method (MMSM) for Tracking the Soot Number Density Function." *Proceedings of the Combustion Institute* 37(1):1041–48.

Zhang, T., Zhao, L., Kholghy, M. R., Thion, S., and Thomson, M. J., 2019. "Detailed investigation of soot formation from jet fuel in a diffusion flame with comprehensive and hybrid chemical mechanisms". *Proceedings of the Combustion Institute*, 37(2):2037–2045.

Zimmer, L., Pereira, F., 2020. "Limitations of simplified models to predict soot formation in laminar flames." *J. Braz. Soc. Mech. Sci. Eng.* 42:340.

8. RESPONSIBILITY NOTICE

The authors are the only responsible for the printed material included in this paper.